Probing Na^+-Induced Changes in the HIV-1 TAR Conformational Dynamics Using NMR Residual Dipolar Couplings: New Insights into the Role of Counterions and Electrostatic Interactions in Adaptive Recognition†

Anette Casiano-Negroni, Xiaoyan Sun, and Hashim M. Al-Hashimi*

Department of Chemistry, Biophysics Research Division, and Program in Bioinformatics, The University of Michigan, 930 North University Avenue, Ann Arbor, Michigan 48109-1055

Received February 16, 2007; Revised Manuscript Received March 31, 2007

ABSTRACT: Many regulatory RNAs undergo large changes in structure upon recognition of proteins and ligands, but the mechanism by which this occurs remains poorly understood. Using NMR residual dipolar coupling (RDCs), we characterized Na^+-induced changes in the structure and dynamics of the bulge-containing HIV-1 transactivation response element (TAR) RNA that mirrors changes induced by small molecules bearing a different number of cationic groups. Increasing the Na^+ concentration from 25 to 320 mM led to a continuous reduction in the average inter-helical bend angle (from 46° to 22°), inter-helical twist angle (from 66° to −18°), and inter-helix flexibility (as measured by an increase in the internal generalized degree of order from 0.56 to 0.74). Similar conformational changes were observed with Mg^{2+}, indicating that nonspecific electrostatic interactions drive the conformational transition, although results also suggest that Na^+ and Mg^{2+} may associate with TAR in distinct modes. The transition can be rationalized on the basis of a population-weighted average of two ensembles comprising an electrostatically relaxed bent and flexible TAR conformation that is weakly associated with counterions and a globally rigid coaxial conformation that has stronger electrostatic potential and association with counterions. The TAR inter-helical orientations that are stabilized by small molecules fall around the metal-induced conformational pathway, indicating that counterions may help predispose the TAR conformation for target recognition. Our results underscore the intricate sensitivity of RNA conformational dynamics to environmental conditions and demonstrate the ability to detect subtle conformational changes using NMR RDCs.

Many regulatory ribonucleic acids (RNAs) undergo large changes in conformation upon binding to proteins and small ligand molecules, but the mechanism by which this occurs remains poorly understood (*1*−*4*). Numerous studies have examined the extent to which molecules induce new RNA conformations versus capture conformations that are dynamically accessible in the unbound state (*1*, *5*−*11*). In contrast, fewer studies have examined the potential role of monovalent and divalent cations in conformational adaptation and target recognition (*12*).

The interaction between the transactivation response element (TAR[1]) RNA (*13*) from the human immunodeficiency type I virus (HIV-1) and the viral transactivator protein (Tat) is a paradigm for understanding the rules of RNA adaptive recognition (*1*, *5*, *8*, *14*) and a primary target for developing anti-HIV therapeutics (*15*−*18*). Several high-resolution structures have been reported for HIV-1 TAR (Figure 1), including the free form (*19*) and bound to divalent cations (*20*), peptide mimics of Tat (*21*, *22*), and six distinct small molecules containing a different number of cationic groups designed to inhibit its interaction with Tat (*23*−*26*). These TAR conformations differ dramatically both in the global orientation of helices (inter-helical bend angle ranging between ∼5° and ∼47°) as well as the local conformation of bulge and neighboring residues where molecules bind. Thus, by adopting different conformations, TAR is capable of binding chemically diverse targets (Figure 1).

The molecular basis for TAR conformational adaptation is key for understanding its role in Tat-mediated transcription elongation of HIV-1 genes and for rationally designing inhibitors of its interaction with Tat (*17*, *18*). Electrostatic interactions play important roles in both RNA folding and recognition (*27*−*32*) and thus can provide a basis for driving conformational changes accompanying complex formation. Previous studies have emphasized the importance of electrostatic interactions in TAR recognition. The spatial arrangements of basic groups in Tat relative to the negative TAR surface is an important determinant of Tat binding and its induced TAR conformational changes (*33*). The Tat bound TAR conformation (*21*, *22*) can be stabilized by distinct small molecules that can satisfy two key electrostatic interactions

† This work was supported by funding from the NIH (RO1 AI066975-01) and the Rackham Science Award (University of Michigan). The Michigan Economic Development Cooperation and the Michigan Technology Tri-Corridor supported and purchased the 600 MHz spectrometer.

* To whom correspondence should be addressed. Tel: (734) 615-3361. Fax: (734) 647-4865. E-mail: hashimi@umich.edu.

[1] Abbreviations: RDC, residual dipolar couplings; HSQC, heteronuclear single quantum coherence spectroscopy; TAR, transactivation response element; HIV, human immunodeficiency virus.

10.1021/bi700335n CCC: $37.00
Published on Web 05/09/2007

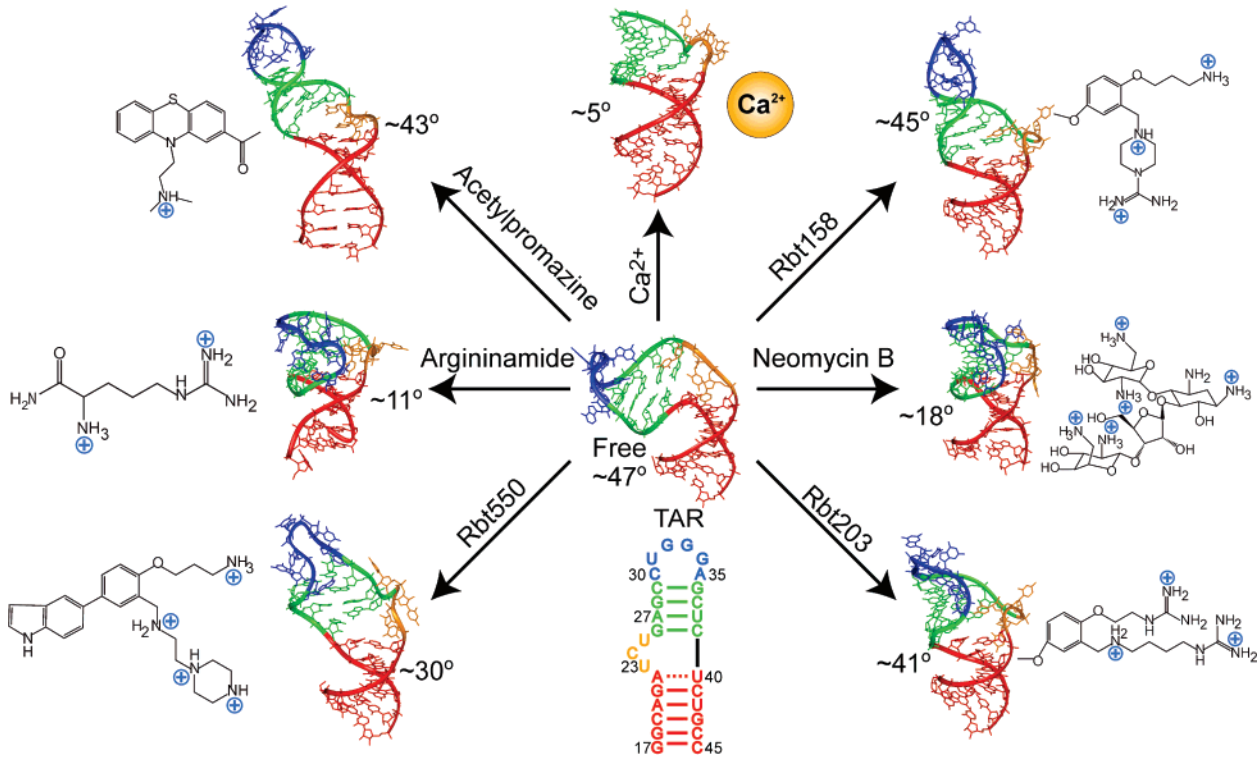

FIGURE 1: Conformation of HIV-1 TAR in free form and bound to distinct molecular targets (*19*, *20*, *22*−*26*). The inter-helical bend angle is indicated next to each conformation.

(*26*). Aminoglycosides bind TAR with affinities that correlate with their total number of positive amines (*34*). Our NMR studies suggest that the changes in the TAR conformational dynamics induced by small molecules are also correlated to their total number of positive groups (*35*).

RNA electrostatic hot spots, which would normally be stabilized by cationic groups on proteins and small molecules, are expected to be energetically unfavorable in the unbound RNA. One can therefore expect that these structural elements only become significantly stabilized during or following complex formation. However, metal cations can also stabilize such electrostatic hot spots and thus pre-adapt the RNA conformation for target recognition. Several studies have shown that a variety of monovalent and divalent cations can associate with the TAR bulge (*20*, *36*−*38*). Transient electric birefringence (*39*) and NMR (*40*) studies have shown that the addition of Mg^{2+} results in a significant reduction in the TAR inter-helical bend angle and dynamics (*20*). However, as is often the case, it remains unclear whether the Mg^{2+}-induced transition is driven by nonspecific electrostatic interactions with diffusive counterions, which could be recapitulated by cationic groups on small molecules, or by inner-sphere contacts with specifically bound metals. Another unresolved question, which has also proven generally difficult to address, is whether the TAR conformations observed at various metal concentrations represent distinct conformations or a dynamical average of two or more states.

A number of studies suggest that the metal-induced TAR structural transition is driven by specific inner sphere contacts. An X-ray structure of TAR shows four specifically bound Ca^{2+} ions that stabilize a unique UCU bulge conformation through several inner-sphere contacts with TAR ligands (*20*). Furthermore, transient electric birefringence studies have shown that Mg^{2+}-induced transitions in bulge containing RNAs are not recapitulated by Na^+ even when using up to 50-fold higher concentrations (*41*). However, EPR studies show that Na^+ and Ca^{2+} induce similar TAR conformational changes (*38*) but that other metals can induce distinct effects (*39*).

Metal-induced RNA conformational transitions have been studied using a variety of experimental biophysical techniques including EPR (*37*, *38*), fluorescence spectroscopy (*42*), hydroxyl radical footprinting (*43*), analytical ultracentrifugation (*44*), small angle X-ray scattering (*45*), and small angle neutron scattering (*46*). Although it can uniquely provide information about both structure and dynamics at site-specific resolution, few studies have employed NMR to structurally characterize metal-induced RNA transitions. This is in part because conventional NOE derived distance restraints can be insensitive to global conformational changes (*47*) and because high-resolution structure determination remains time consuming, which makes characterizing structures at multiple metal concentrations impractical (*48*, *49*).

In this study, we exploit the exquisite conformational sensitivity of NMR residual dipolar couplings (RDCs) (*50*−*53*) to characterize how the structure and dynamics of TAR change as a function of increasing Na^+ concentration and compare findings with changes induced by Mg^{2+} and small molecules. Aiding our study is an order tensor based analysis of RDCs that permits studies of global conformational dynamics with high efficiency (*14*, *48*, *49*, *54*, *55*). The RDCs allowed us to detect Na^+-induced changes in the TAR conformation that are indistinguishable from those induced by Mg^{2+}, even though chemical shift mapping data suggest that the two metals may bind TAR using distinct modes. These results together with electrostatic calculations offer

new insights into the possible role of electrostatic interactions and counterion condensation in TAR adaptive recognition.

MATERIALS AND METHODS

NMR Sample Preparation. Samples of uniformly $^{13}C/^{15}N$ labeled TAR were prepared by *in vitro* transcription using synthetic double stranded DNA templates containing the T7 promoter and sequence of interest (Integrated DNA Technologies, Inc.), T7 RNA polymerase (Takara Mirus Bio, Inc.), and $^{13}C/^{15}N$ labeled nucleotide triphosphates (ISOTEC, Inc.). The RNA was purified by 20% (w/v) denaturing polyacrylamide gel electrophoresis containing 8 M urea and 1× TBE followed by electroelution in 20 mM Tris (pH 8) buffer and ethanol precipitation. The RNA pellet was dissolved and exchanged into NMR buffer (15 mM sodium phosphate, 0.1 mM EDTA, and 25 mM NaCl at pH ~6.4,) using a centricon ultracel YM-3 concentrator (Millipore Corp.). The final RNA concentration in the aligned NMR samples was 0.3/0.5 mM for Na^+/Mg^{2+}, respectively. Three separate samples were used to measure RDCs at 160 and 320 mM Na^+, and 25 mM Na^+/4 mM Mg^{2+}. The aligned samples were prepared by adding Pf1 phage (50 mg/mL) (*56*, *57*) in NMR buffer to a preconcentrated TAR RNA sample to yield a final Pf1 phage concentration of 17−20 mg/mL. The addition of phage did not affect the effective Na^+ or Mg^{2+} concentration as judged from careful comparison of the chemical shifts in the absence and presence of phage (see Supporting Information).

Measurement of RDCs. All NMR experiments were performed at 298 K on an Avance Bruker 600 MHz spectrometer equipped with a triple resonance cryogenic (5 mm) probe with the exception of the 320 mM Na^+ RDCs, which were measured on a Varian Inova 800 MHz spectrometer equipped with a triple resonance Z-gradient probe. NMR spectra were analyzed using NMR Draw (*58*) or Felix (Accelrys Inc., 2002) and overlaid in Sparky 3 (*59*). The measurement of RDCs in 25 mM NaCl (*14*) and in the presence of Mg^{2+} (*40*) have been reported previously. The measurements of RDCs in the presence of Mg^{2+} (0.5 mM RNA and 25 mM Na^+/4 mM Mg^{2+}) were repeated using the same experiments and conditions used for the Na^+ RDC measurements. The results were consistent with previous values (*40*). One bond $^1D_{C6H6}$, $^1D_{C8H8}$, $^1D_{C5H5}$, $^1D_{C2H2}$, $^1D_{C1'H1'}$, and $^1D_{N1/3H1/3}$ RDCs were measured using 2D ^{13}C-^1H (or ^{15}N-^1H) S^3E HSQC experiments (*35*, *60*) from the difference in splittings measured along the ^{13}C (or ^{15}N) dimension observed in the presence and absence of Pf1 phage (*56*, *57*). The RDC measurement error was estimated from duplicate measurements using experiments that yield splittings along the ^1H and $^{13}C/^{15}N$ dimension (standard deviation between two RDC sets was 0.9 Hz). The measured RDCs are listed in Supporting Information.

Chemical Shift Mapping. 2D HSQC spectra were recorded following incremental increases in $[Na^+]$ (25, 40, 80, 160, and 320 mM against 0.2 mM TAR) or $[Mg^{2+}]$ (0, 0.2, 0.4, 0.8, 1.6, 3.2, and 6.4 mM against 0.2 mM TAR). Apparent dissociation constants (K_d) were obtained by fitting the observed changes in chemical shift to the following equation (*65*):

$$\delta_{obs} = \delta_{Free} + \frac{(\Delta\delta_T)\{([M]_T + [RNA]_T + K_d) - \sqrt{([M]_T + [RNA]_T + K_d)^2 + (4[M]_T[RNA]_T)}\}}{2[RNA]_T} \quad (1)$$

where $[M]_T$ is the total concentration of metal (Na^+ or Mg^{2+}), $[RNA]_T$ is the TAR concentration based on UV absorbance at 260 nm, $\Delta\delta_T$ is the difference in chemical shifts between the free and metal associated states (in ppm), δ_{obs} is the observed chemical shift (in ppm), and δ_{Free} is the chemical shift in the free state (in ppm). The data was fitted using the Origin software (OriginLab Corporation) in which $\Delta\delta_T$ and K_d (and δ_{Free} for Na^+) were allowed to vary during the fit. The K_d errors obtained from the fit were in excellent agreement with values obtained independently using a Monte Carlo approach. For the latter, residuals corresponding to the difference between the measured and best-fitted chemical shifts in the titration curves were computed for all fitted data. The resulting distribution of residuals was fitted to a Gaussian distribution. Next, simulations were performed in which perfect chemical shift titration data points corresponding to experimental values were generated and each point perturbed by a value randomly chosen from the Gaussian distribution. The perturbed points were then fitted to eq 1 and the calculations repeated 100 times. The difference between the true K_d values used in the simulation and the values obtained from curve-fitting were then fitted to a Gaussian distribution and the resulting standard deviation assumed to be the K_d error.

Order Tensor Analysis of RDCs. The RDCs measured in the TAR helices were subjected to an order tensor analysis using idealized A-form helices as input coordinates (*14*), as implemented in the program AFORM-RDC (*55*). The helices were constructed using the Biopolymer module in Insight II (Molecular Simulations, Inc.) followed by correction of propeller twist angles from +15° to −15° (*61*). The measured RDCs were fitted to idealized A-form helices using singular value decomposition (*62*) implemented in the in-house written program RAMAH (*63*). RDCs from terminal residues (17, 45, 22, and 40), bulge residues (23−25), and hairpin loop residues (31−34) were excluded from the analysis. The order tensor errors due to parametrized A-form structural noise and RDC uncertainty were estimated using the program AFORM-RDC (*55*). Key statistics for the order tensor analysis are summarized in Table 1.

For each metal condition, helices were rotated into the principal axis system (PAS) of their best-fitted order tensor and assembled using the program Insight II (Molecular Simulations, Inc) by linking U40 (P) to C39 (O3′) (~1.59 Å). Because of the order tensor degeneracy (*64*), this yielded four possible inter-helical orientations, three of which could be discarded: two because they lead to antiparallel helix alignments and one because it resulted in a distance between A22 (O3′) and G26 (P) (>30 Å) that cannot be satisfactorily linked using the trinucleotide bulge. Inter-helical angles for all TAR structures were calculated using an in-house program.

Electrostatic Calculations. HIV-1 TAR RNA structures in free form (pdb ID# 1ANR) and bound to argininamide (pdb ID# 1ARJ), Ca^{2+} (pdb ID# 397D), acetylpromazine

Table 1: Order Tensor Analysis of TAR RDCs Measured under Different Metal Conditions[a]

metal condition	stem	N	CN	rmsd (Hz)	R	η	$\vartheta \times 10^{-3}$	ϑ_{int}	θ(°)	ξ(°)
25 mM	I	13	2.9	1.1	0.99	0.27 ± 0.04	0.48 ± 0.04	0.56 ± 0.05	46 ± 4	61 ± 50
NaCl	II	11	3.1	1.1	0.99	0.11 ± 0.07	0.88 ± 0.04			
160 mM	I	15	2.9	1.3	0.99	0.15 ± 0.03	0.57 ± 0.03	0.67 ± 0.05	37 ± 7	−1 ± 50
NaCl	II	14	4.2	1.2	0.99	0.15 ± 0.04	0.85 ± 0.04			
320 mM	I	12	2.8	1.5	0.98	0.23 ± 0.04	0.67 ± 0.04	0.74 ± 0.08	22 ± 7	−18 ± 50
NaCl	II	12	4.0	1.1	0.99	0.20 ± 0.04	0.90 ± 0.08			
4 mM	I	13	2.9	1.0	0.99	0.26 ± 0.04	0.80 ± 0.03	0.85 ± 0.04	17 ± 7	−58 ± 50
$MgCl_2$	II	14	4.1	1.0	0.99	0.17 ± 0.08	0.94 ± 0.03			

[a] Shown for each helical stem are the number of RDCs (*N*), the condition number (*CN*) (*69*) describing the orientational spread of the RDC targeted bond vectors, the root-mean-square deviation (rmsd), the correlation coefficient (*R*) between measured and back-predicted RDCs, the order tensor asymmetry ($\eta = |S_{yy} - S_{xx}|/S_{zz}$), generalized degree of order (ϑ), internal generalized degree of order (ϑ_{int}), inter-helical bend (θ), and twist (ξ) angles. Errors are estimated using the program AFORM-RDC.

(pdb ID# 1LVJ), neomycin B (pdb ID# 1QD3), Rbt158 (pdb ID# 1UUI), Rbt203 (pdb ID# 1UUD), and Rbt550 (pdb ID# UTS1) were obtained from the Protein Data Bank and used in the analysis. Electrostatic calculations were performed by solving the nonlinear Poisson−Boltzmann equation using the Delphi (*66*) module of Insight II (Molecular Simulations, Inc.). No bound waters, ions, or ligands were included in the calculation. The DNA−RNA AMBER force field (*67*) was used for partial charges of atoms. An interior dielectric constant of 2 was used for the RNA molecule. The continuum dielectric constant for the solvent (water) was set to 80 with a 1:1 electrolyte distribution according to the Boltzmann weighted average of the mean potential. A 2.0 Å exclusion radius was added to the surface of the RNA to account for ion size and a 1.4 Å probe used to determine the RNA molecular surface. A monovalent salt concentration of 0.025 M was used in the calculations to mimic the low ionic strength NMR conditions. Three dimensional structures were mapped onto a grid (65 × 65 × 65 grid points/side) and the boundary potential at each lattice was calculated using the Debye−Huckel and full Columbic equations implemented in Delphi (*66*). The calculated electrostatic potential maps were displayed using the program GRASP provided by the Honig lab (*66*).

RESULTS AND DISCUSSION

Chemical Shift Mapping of Na^+ and Mg^{2+} Association with TAR RNA. As shown in Figure 2A, large and specific changes in chemical shift were observed in 2D HSQC spectra of TAR (0.3 mM) upon incrementally increasing the NaCl concentration from 25 to 320 mM in a background buffer containing 15 mM sodium phosphate and 0.1 mM EDTA at pH ~6.4. The largest chemical shift changes were observed in and around the bulge. In contrast, little to no changes were observed for residues in the UUCG loop. For the majority of resonances, the directions of the chemical shift perturbations were similar to those induced by Mg^{2+} although the magnitude of the latter was uniformly larger (Figure 2A). As shown in Figure 2B, fitting of the chemical shift titration data to a two-state model yields apparent K_d values that are more than two orders of magnitude smaller for Mg^{2+} (K_d ~0.074 ± 0.002 − 0.10 ± 0.01 mM) compared to that for Na^+ (K_d ~0.11 ± 0.01 − 0.28 ± 0.09 M) as has been reported for other RNAs. No further changes in the TAR chemical shifts were apparent beyond 6.4 mM Mg^{2+}, which is consistent with saturation kinetics and specific metal-induced transition. In the case of Na^+, chemical shift data could not be recorded near saturation point as this would require salt concentrations (~1 M) outside the tuning capacity of our probe.

Despite many similarities, subtle but detectable differences between the Mg^{2+} and Na^+ chemical shift perturbations were observed for residues G26, U23, and A27 (highlighted with a box, Figure 2A). Significantly, these are precisely the residues that are involved in inner sphere contacts with Ca^{2+} cations in the X-ray structure of TAR (*20*). Thus, Na^+ and Mg^{2+} either stabilize a different conformation for these residues and/or associate with them in a different manner.

Structure and Dynamics of TAR as a Function of Na^+ and Mg^{2+} Using RDCs. The interpretation of chemical shift perturbations is complicated by the fact that they are sensitive to changes in structure, dynamics, and metal localization. To specifically characterize the metal-induced TAR conformational changes, we measured RDCs in TAR (0.3 mM) at Na^+ concentrations of 25, 160, and 320 mM. On the basis of the apparent K_d values (Figure 2B), these correspond to 10%, 43%, and 60% of TAR being in the Na^+ bound state. For comparison, RDCs in the presence of 25 mM Na^+/4 mM Mg^{2+} (83% of TAR bound) were measured using the same NMR experiments and sample conditions used to measure the Na^+ RDCs. The Mg^{2+} RDCs were measured slightly below saturation, allowing insight into the dynamical nature of the metal-induced TAR transition under physiological Mg^{2+} concentrations. The Mg^{2+} RDCs were in very good agreement with values reported previously at slightly different Mg^{2+} concentrations (*40*).

As shown in Figure 3A, continuous and significant changes in RDCs (normalized for differences in total degree of order; see Figure 3 legend) were observed upon increasing the Na^+ concentration, providing strong evidence for Na^+-induced changes in the TAR conformation. The 320 mM Na^+ RDCs are in better agreement with those measured at 25 mM Na^+ in the presence rather than in the absence of 4 mM Mg^{2+} (Figure 3A), indicating that Na^+ and Mg^{2+} induce similar TAR conformational changes.

To further characterize the metal-induced transition, the RDCs were subjected to an order tensor analysis (*62*, *68*, *69*). Here, non-terminal Watson−Crick (WC) base pairs in individual helical stems were modeled assuming an idealized A-form geometry (*14*, *54*, *55*). The RDCs and idealized A-form geometry were then used to determine order tensors for each helical stem (statistics summarized in Table 1). As shown in Figure 3B, an excellent order tensor fit was obtained for RDCs measured under all metal conditions

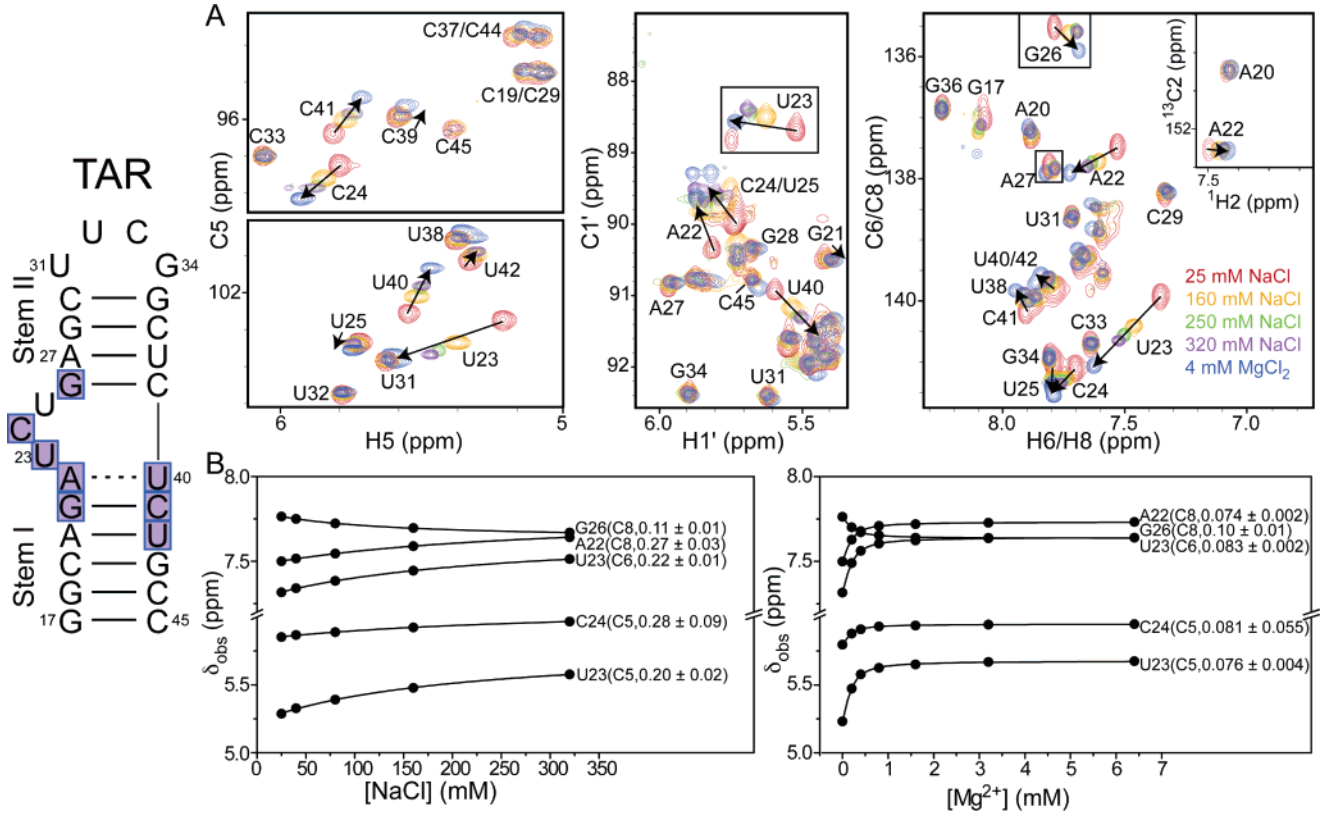

FIGURE 2: Chemical shift mapping of Na^+ and Mg^{2+} association with TAR RNA. On the left, the secondary structure of the TAR construct used in this study is shown. The wild-type loop is replaced with a UUCG loop. (A) 2D HSQC spectra of TAR recorded in the presence of Na^+ (25, 160, and 320 mM) and Mg^{2+} (25 mM Na^+/4 mM Mg^{2+}). Residues undergoing the largest chemical shift perturbations (top 20% for a given type of resonance) upon Na^+ and Mg^{2+} binding are highlighted in blue and purple square boxes, respectively, on the TAR secondary structure. (B) Representative Na^+ and Mg^{2+} titration curves with K_d values (in M for Na^+ and in mM for Mg^{2+}) shown at the end of each curve.

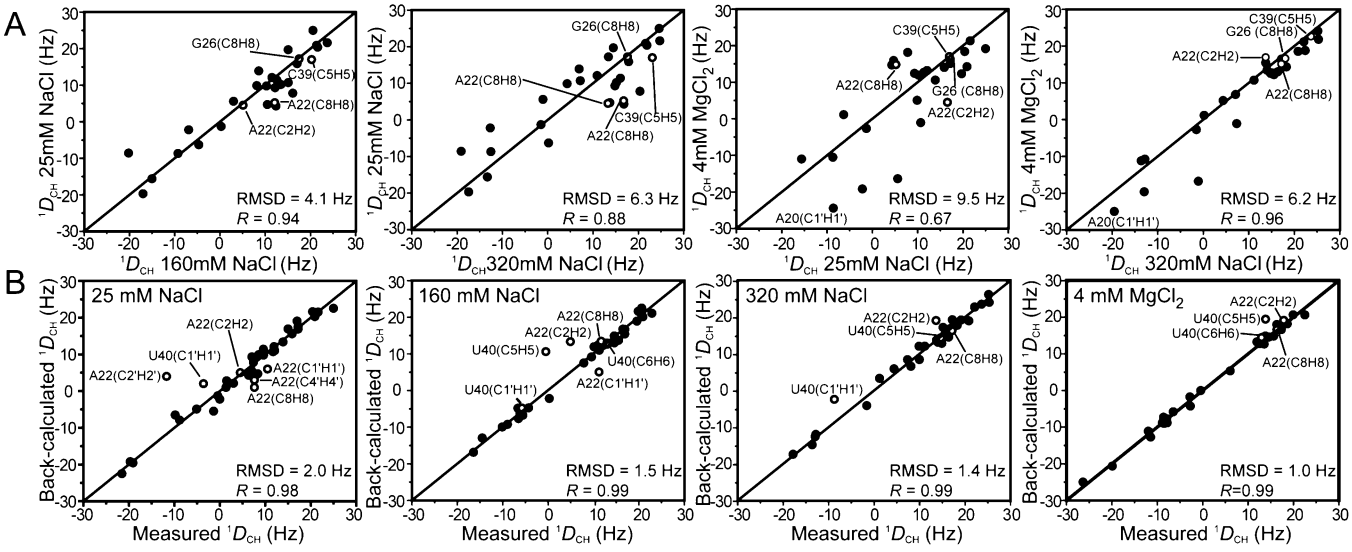

FIGURE 3: (A) Comparison of RDCs measured at 25, 160, and 320 mM Na^+ and Mg^{2+} (25 mM Na^+/4 mM Mg^{2+}). The RDCs are normalized (relative to 25 mM Na^+) to account for differences in the degree of order. This was done by scaling the RDCs measured under salt condition "X" by the ratio of stem II degree of order measured at X and 25 mM (i.e., through multiplication by $\vartheta_{Na-25mM}/\vartheta_X$). Stem II was chosen because it dominates the total degree of alignment in all cases (Table 1). (B) Order tensor fits against an idealized A-form geometry carried out independently for stems I and II using RDCs measured at 25, 160, and 320 mM Na^+ and 25 mM Na^+/4 mM Mg^{2+}. Shown in each case is the root-mean-square deviation (rmsd) between measured and back-predicted RDCs as well as the correlation coefficient (R).

examined. In all cases, the root-mean-square deviation (rmsd) between measured and back-predicted RDCs compared favorably with the RDC measurement uncertainty (0.9 Hz SD from comparison of ^1H and ^{13}C dimension RDCs). Thus, the local conformation of the WC pairs does not vary significantly from the ideal A-form geometry. The excellent RDC fits observed for residues G26 and A27 argue that the observed chemical shift differences with Na^+ and Mg^{2+} (Figure 2A) are not likely due to different metal-induced conformational changes at these sites but rather to differences

in the modes of metal association with TAR. Likewise, both Na^+ and Mg^{2+} yield slightly reduced values in the already attenuated bulge RDCs, particularly for U23 (see Supporting Information). As mentioned previously (*40*), this is consistent with an increase in the local flexibility accompanying looped-out bulge residues (*20*). The agreement for the flexible terminal A22-U40 base pair RDCs (*14*, *40*) (shown as open symbols, Figure 3), which were not included in the order tensor fit, improves with increasing metal concentration (rmsd = 6.9, 5.1, and 3.4 Hz at 160 and 320 mM Na^+ and 25 mM Na^+/4 mM Mg^{2+}, respectively). This stabilization is consistent with the observed increase in coaxial stacking between the two stems with increasing metal concentration (see below).

Given the excellent fit to the A-form geometry, the observed changes in RDCs with increasing Na^+ concentration must be attributed to changes in the global orientation and/or dynamics of the two helices. To this end, we used the order tensors computed for each helix to determine their relative orientation and dynamics (*62*, *68*) with estimated errors calculated using the program AFORM-RDC, which yields order tensor errors due to a combination of A-form structural noise and RDC uncertainty (*55*). In this analysis, the relative orientation of helices is obtained by superimposing their order tensor frames describing helix alignment relative to the applied magnetic field. The amplitude of inter-helical motions is computed from the ratio of the generalized degree of order ($\vartheta_{int} = \vartheta_i/\vartheta_j$; $\vartheta_i < \vartheta_j$) describing the degree of helix alignment relative to the applied magnetic field (*14*, *69*). The ϑ_{int} value ranges between 1 for inter-helical rigidity and 0 for maximum inter-helical motions. Owing to possible correlations between helix motions and overall alignment, the ϑ_{int} value will generally underestimate the real motional amplitudes (*14*, *70*).

As shown in Figure 4, increasing the Na^+ concentration from 25 to 320 mM led to a gradual reduction in the inter-helical bend from $\theta = 46 \pm 4°$ to $22 \pm 7°$ (Figure 4A). This was accompanied by a reduction in the inter-helical twist angle from $\xi = 66 \pm 50°$ to $-18 \pm 50°$ (Figure 4B) and amplitude of inter-helical motions from $\vartheta_{int} = 0.59 \pm 0.06$ to 0.74 ± 0.08 (Figure 4C). Assuming an isotropic cone motional model (*13*), the ϑ_{int} values correspond to inter-helical motional amplitudes of 48°, 41°, and 35° at Na^+ concentrations of 25, 160, and 320 mM respectively. The comparatively large error in the inter-helical twist angle reflects the larger uncertainty in the principal $S_{xx}-S_{yy}$ directions arising due to near axial symmetry ($\eta \sim 0$) of the helix order tensors (Table 1). Similar but significantly larger conformational changes were induced by 25 mM Na^+/4 mM Mg^{2+} ($\theta = 17 \pm 7°$, $\xi = -58 \pm 50$, and $\vartheta_{int} = 0.85 \pm 0.04$, shown as horizontal lines in Figure 4). This suggests that the similar Na^+- and Mg^{2+}-induced TAR chemical shift perturbations (Figure 2A) likely reflect a similar TAR conformational change that is driven by nonspecific electrostatic interactions with counterions.

Two State Nonspecific Electrostatic Switch Underlies the Metal-Induced TAR Structure−Dynamical Transition. The TAR conformations observed at 25, 160, and 320 mM Na^+ and 25 mM Na^+/4 mM Mg^{2+} may either represent distinct conformations or a population weighted average of two or more conformational states. Although these scenarios can be difficult to resolve (*46*), the latter can be tested for a

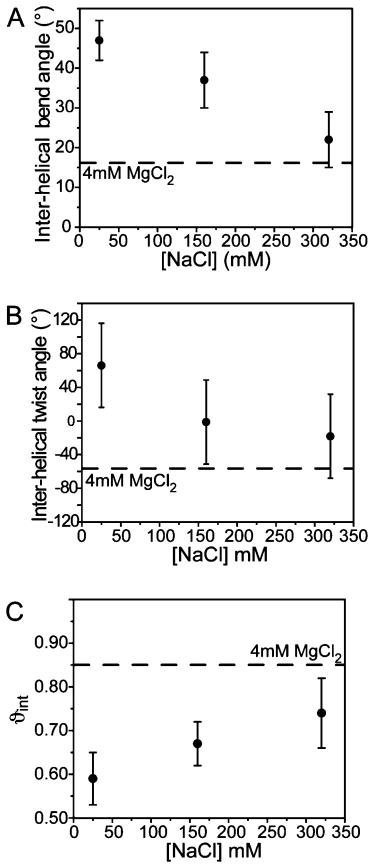

FIGURE 4: Probing the metal-induced TAR structure−dynamical transition using an order tensor analysis of RDCs. Shown are the (A) inter-helical bend angle (θ), (B) inter-helical twist angle (ξ) (positive/negative values correspond to over/under twisting, respectively), and (C) inter-helical mobility (ϑ_{int}) as a function of Na^+ concentration. Values in the presence of 25 mM Na^+/4 mM Mg^{2+} are shown using a horizontal line.

simple two-state phenomenological model that is consistent with an apparent good fit of chemical shift perturbations to a two state model (Figure 2B). Here, it is assumed that TAR consists of a population weighted average of two states: a metal free ensemble, characterized by an inter-helical bend angle θ(free) and inter-helical flexibility ϑ_{int}(free) that is weakly associated with metals and that is favored at low ionic strength conditions (Figure 5A). The metal bound state, characterized by inter-helical bend angle θ(bound) and inter-helical flexibility ϑ_{int}(bound), is more strongly associated with metals and, within our metal concentration range, is favored at high ionic strength conditions (Figure 5A). Assuming that the dynamical interconversion between the free and bound states occurs at timescales faster than the inverse of the measured RDCs (i.e., faster than milliseconds), the observed RDCs will be a population weighted average over the two states. Simulations using the TAR helices (data not shown) show that to a good approximation, the observed ϑ_{int} (ϑ_{int}-(obs)) and inter-helical bend angle (θ(obs)) at a given Na^+ (or Mg^{2+}) will be given by a population weighted average of free and bound ensembles (*40*, *71*) as follows:

$$\theta(\text{obs}) = (1 - p_{\text{bound}}) \times \theta(\text{free}) + p_{\text{bound}} \times \theta(\text{bound}) \quad (2)$$

$$\vartheta_{\text{int}}(\text{obs}) = (1 - p_{\text{bound}}) \times \vartheta_{\text{int}}(\text{free}) + p_{\text{bound}} \times \vartheta_{\text{int}}(\text{bound})$$

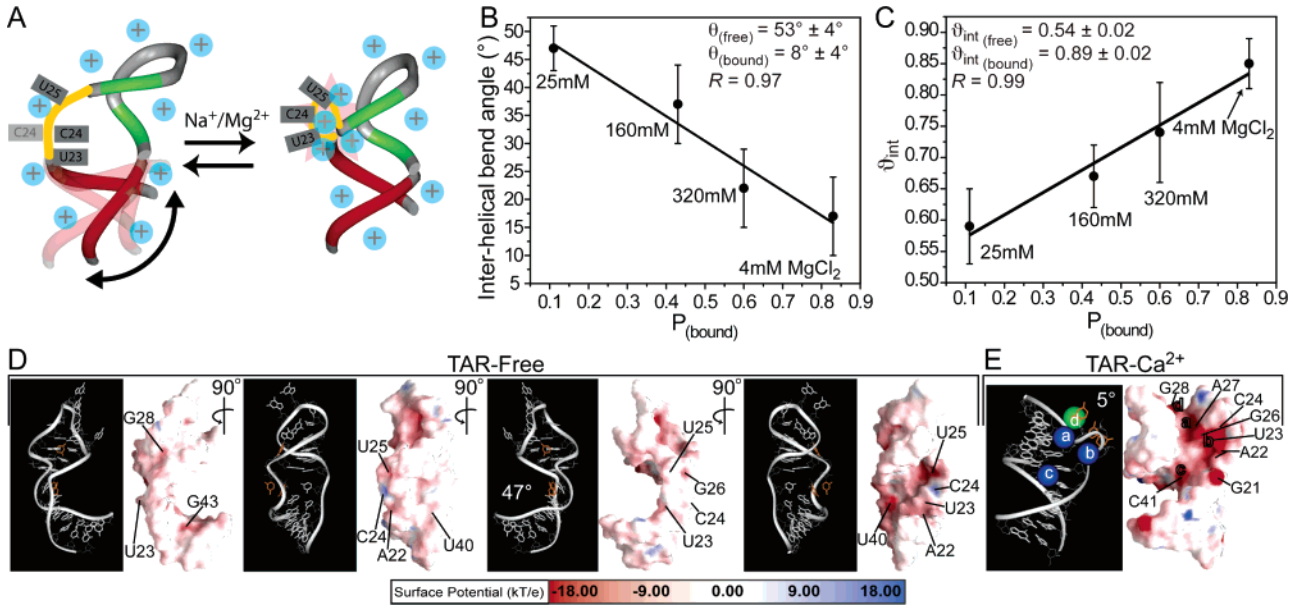

FIGURE 5: (A) Two-state model for the metal-induced TAR structural transition. (B−C) Fitting of the observed (B) inter-helical bend angle (θ(obs)) and (C) amplitude of inter-helical motions (ϑ_{int}(obs) as a function of the fractional bound populations (p_{bound}) using eq 2. The free and bound θ and ϑ_{int} values obtained from the fit are shown together with the correlation coefficient (R). (D−E) Electrostatic surfaces for TAR (D) in free form (pdb ID# 1ANR) (*19*), under moderate ionic strength conditions (50 mM NaCl and 5 mM phosphate buffer) with different views showing the weaker electrostatic potential, and (E) bound to Ca^{2+} cations (pdb ID# 397D) (*20*) with residues undergoing the largest metal-induced chemical shift perturbations highlighted.

where the values of p_{bound} can be computed from the apparent K_d values determined for Na^+ and Mg^{2+} on the basis of the chemical shift titrations (Figure 2B). Assuming that Mg^{2+} stabilizes a similar bound structure as Na^+, which is supported by RDC measurements (Figure 3), the ϑ_{int}(obs) and θ(obs) measured under all four metal conditions (25, 160, and 320 mM Na^+ and 25 mM Na^+/4 mM Mg^{2+}) can be fitted to eq 2 to solve for the two unknowns in each case (ϑ_{int}(free), ϑ_{int}(bound) and θ(free), θ(bound), respectively).

As shown in Figure 5, a good fit can be obtained for both the inter-helical bend angle θ(obs) (Figure 5B) and flexibility ϑ_{int}(obs) (Figure 5C). The average K_d values obtained for the largest chemical perturbations (see Materials and Methods) were used in computing p_{bound}, with minor differences observed when using various K_d values from the range observed (Figure 2B). No attempts were made to fit the inter-helical twist angles given their much larger uncertainty. The fit yields parameters for the metal bound state (ϑ_{int}(bound) = 0.89 ± 0.02 and θ(bound) = 8° ± 4°) that are in very good agreement with expectations based on the X-ray structure of TAR (θ(bound) = −11° and (ϑ_{int}(bound) = 1.0), which was determined in the presence of saturating amounts of divalent ions (100 mM $CaCl_2$) (*20*).

Model conformations for the free and bound TAR states have been reported, namely, an NOE-based NMR structure of unbound TAR under low ionic strength conditions in the absence of divalent ions (50 mM NaCl and 5 mM phosphate buffer) (*19*) and an X-ray structure of TAR determined in the presence of saturating Ca^{2+} concentrations (100 mM $CaCl_2$, 50 mM Na-cacodylate, and 200 mM NH_4Cl) (*20*). To gain insight into the molecular basis for the metal-induced structural transition, we performed nonlinear Poisson−Boltzmann calculations (*27*, *66*) and compared the surface electrostatic potential for these two TAR conformations. The negative electrostatic potential was significantly weaker for the unbound TAR structure (Figure 5D). Here, inter-helical bending allows the bulge to adopt an extended conformation that minimizes negative charge repulsion while allowing U23 to adopt a looped in stacked conformation (*19*) (Figure 5A). The looping in of this bulge residue accounts for the overtwisting observed at low ionic strength (+ve ξ angles, Figure 4B) (*19*). In stark contrast, as shown in Figure 5E, a strong negative electrostatic potential was observed for the Ca^{2+} bound TAR structure in and around the bulge (G21-C24, and A27) precisely at residues that exhibit large metal-induced chemical shift perturbations (Figure 2A). This strong negative potential explains in part why coaxial TAR conformations are not favored at low ionic strength conditions. Despite the energetic benefits of helical stacking, metals are required to screen repulsive forces. The metal bound TAR conformation is also likely disfavored by the looping out of U23 and the loss of stacking interactions with A22 and U24 (Figure 5A).

Comparison with Small Molecule Binding. We previously used RDCs to characterize the conformational dynamics of TAR bound to the small molecules argininamide (*72*), acetylpromazine, and neomycin B (*35*). We noted qualitatively that the small molecules induce a reduction in the TAR inter-helical bend angle and dynamics by an amount that is apparently dependent on the total number of positive groups. These trends are shown more quantitatively in Figure 6 using an expanded set of TAR structures. An inverse correlation is apparent between the TAR inter-helical bend angle (θ) (Figure 6A) and dynamics (ϑ_{int}) (Figure 6C) and the net positive charge delivered by the small molecule. This is analogous to the trend observed with increasing metal concentration (Figure 4). In contrast, no significant correlation is observed with the inter-helical twist (ξ) angle (Figure 6B), which as mentioned previously is also influenced by the local bulge conformation. For the Tat mimic argininamide (ARG), charges of both +2 and +6 are shown. The latter is based on surface plasmon resonance measurements indicating

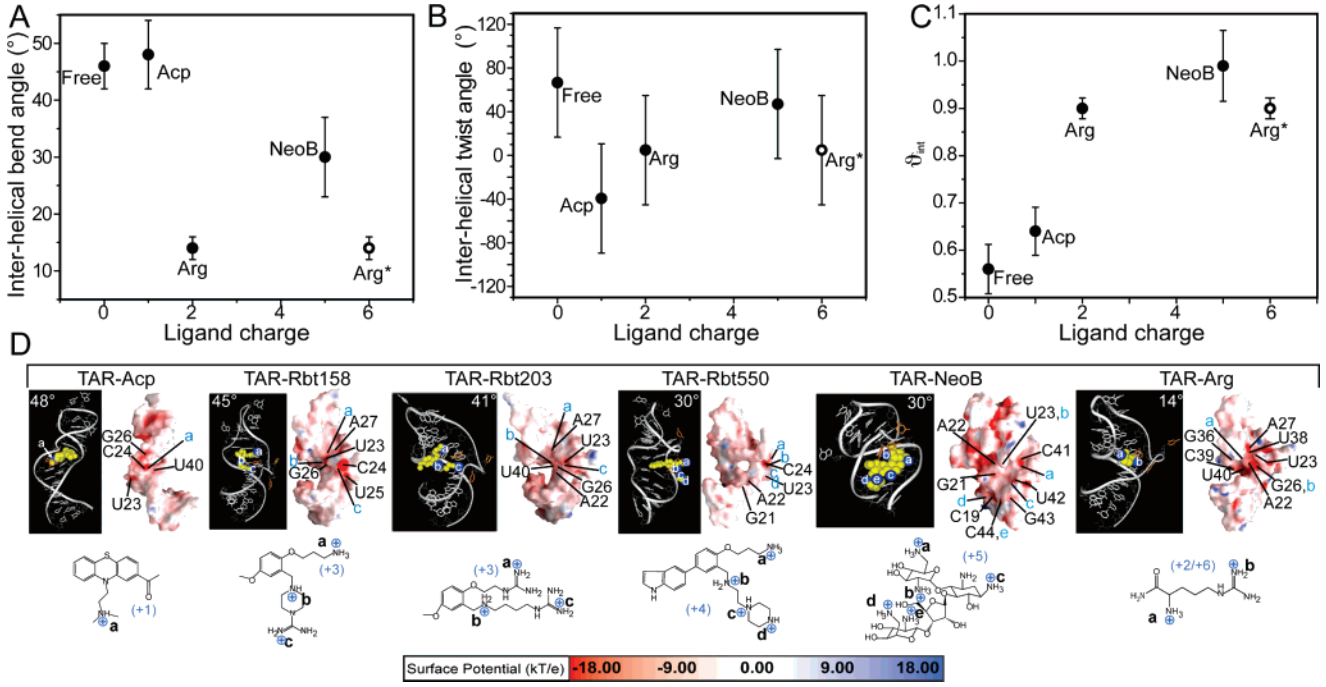

FIGURE 6: TAR conformational dynamics when bound to the small molecules argininamide (ARG), acetylpromazine (ACP), neomycin B (NeoB), Rbt 158, Rbt 203, and Rbt 550. Shown are the (A) inter-helical bend angle (θ), (B) inter-helical twist angle (ξ), and (C) amplitude of inter-helical motions (ϑ_{int}) as a function of total positive charge delivered by the small molecules. The inter-helical bend angles for ARG, ACP, and NeoB were obtained from order tensor analysis of RDCs, as reported previously (*35*, *72*). For the remaining structures, the angles were obtained from model 1 of the NOE-based NMR structure (Rbt 158, Rbt 203, and Rbt 550) (*25*, *26*) or the X-ray structure (Ca^{2+}) (*20*). For ARG, which has a charge of +2, a total charge of +6 is also shown on the basis of surface plasmon resonance measurements that indicate that up to three ARG molecules bind TAR (*26*). For Ca^{2+}, a charge of +8 is assumed on the basis of the observation of 4 × Ca^{2+} ions in the X-ray structure (*20*). (D) Electrostatic surfaces for the bound TAR structures following the removal of ligands. Highlighted in blue letters are the positions of cationic groups on small molecules relative to the TAR electrostatic surface. The TAR orientation in each case was chosen to illustrate the proximity of cationic groups near the strong negative TAR charge potential.

that up to three ARG molecules bind TAR under NMR conditions (*26*).

The above results suggest that electrostatic interactions also dominate the TAR global conformational changes that are induced by small molecule recognition. To explore this further, we performed nonlinear Poisson−Boltzmann calculations on the TAR complexes following removal of bound ligands. Despite variations due to the structural uncertainty of the NMR ensemble (see Supporting Information), cationic groups from small molecules were frequently observed near TAR regions of strong electrostatic potential (Figure 6D), particularly for regions in and around the bulge, as previously noted for the Rbt family of ligands (*26*). Furthermore, as expected, linear TAR conformations (e.g., TAR-NeoB, TAR-Ca^{2+}, and TAR-ARG) generally have a stronger electrostatic potential compared to that of the more bent conformations (e.g., TAR-ACP) (Figure 6D). The electrostatic hot spots in the linear conformations are primarily composed of backbone phosphates (O1P and O2P), which explains why, for example, Mg^{2+}, NeoB, and ARG are effective at stabilizing the TAR global backbone conformation. In contrast, for the highly bent conformations (TAR-ACP, TAR-Rbt158, and TAR-Rbt203), they are primarily composed of oxygen and nitrogen atoms in sugar (O2′, O3′, and O5′) and base (U(O4, O2), G(N7, O6), and A(N7)) moieties. The lack of involvement of backbone phosphates helps rationalize why ACP is ineffective at stabilizing the TAR overall conformation. No dynamical data has been obtained for the Rbt family of small molecules.

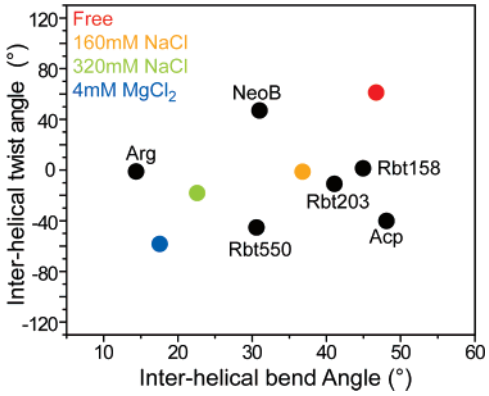

FIGURE 7: Comparison of metal and small molecule-induced changes in the TAR inter-helical conformation.

Possible Role for Counterions in TAR Adaptive Recognition. In Figure 7, we show the inter-helical bend (θ) and twist angles (ξ) for TAR in different ligand bound states along with the conformational changes that are induced by metals ions. Many of the ligand bound TAR conformations fall along or near the predicted two-state metal-induced conformational transition. This highlights the similar changes in the TAR conformation that are induced by small molecules and metals. The largest deviation from the pathway is observed for ACP, which among the bound TAR conformations has the weakest electrostatic potential composed of sugar and base moieties. Interestingly, at the extremity of our two state metal transition, we find the functionally relevant TAR conformation that is stabilized by the Tat mimic ARG (Figure 7). Thus, metals may act to increase

the probability of sampling productive conformations that mimic the functional protein bound state by screening unfavorable backbone repulsive forces. By also reducing the population of nonproductive conformations, counterions may decrease the likelihood for nonspecific adaptation and promiscuous recognition. In this context, metals may act to bias the specificity of internal motions toward functionally active conformations.

CONCLUSIONS

Our results show that Na^+ and Mg^{2+} ions induce a similar TAR structural and dynamical transition from a bent flexible to coaxial rigid state, though the binding modes of the two metals may be different. This is in contrast to previous transient electric birefringence studies indicating that the Mg^{2+}-induced transitions in model bulge-containing RNAs are not reproduced by Na^+ even when using up to 50-fold higher concentrations (*41*). It remains to be established if the observed effects of monovalent ions on the TAR conformation are a general feature of bulge-containing RNAs.

The similar structural and dynamical changes induced by Na^+ and Mg^{2+} strongly suggest that nonspecific electrostatic interactions with diffusive counterions, and not specifically bound metals observed in the X-ray structure, drive the TAR global structure−dynamical transition. Our results do not, however, rule out the presence of inner sphere contact(s), particularly with Mg^{2+}. Similar electrostatic interactions seem to dominate the TAR conformational transitions that are induced by Tat derived peptides and other small molecules. Many of these ligand bound TAR conformations fall near the pathway of the metal-induced conformational transition (Figure 7), suggesting that metals may be involved in adapting the TAR conformation for target recognition.

Finally, our study underscores the intricate sensitivity of RNA structural dynamics to environmental conditions. The range of ionic strength (25−320 mM) over which significant changes in the TAR structural and dynamical changes could be detected falls within a range of buffer conditions that is often used interchangeably. Our results also demonstrate the ability to use RDCs to quantitatively measure subtle differences in RNA conformational dynamics.

ACKNOWLEDGMENT

We thank members of the Al-Hashimi lab, especially Qi Zhang, for insightful comments and help, and Dr. Alex Kurochkin for maintenance of the NMR instruments.

SUPPORTING INFORMATION AVAILABLE

Figures showing bulge RDCs as a function of ionic strength, RDC measurement error, simulations assessing two-state averaging of RDCs, comparison of spectra with and without phage, and electrostatic surfaces for various models of the NMR ensemble. This material is available free of charge via the Internet at http://pubs.acs.org.

REFERENCES

1. Leulliot, N., and Varani, G. (2001) Current topics in RNA-protein recognition: Control of specificity and biological function through induced fit and conformational capture, *Biochemistry 40*, 7947−7956.
2. Micura, R., and Hobartner, C. (2003) On secondary structure rearrangements and equilibria of small RNAs, *ChemBioChem 4*, 984−990.
3. Al-Hashimi, H. M. (2005) Dynamics-based amplification of RNA function and its characterization by using NMR spectroscopy, *ChemBioChem 6*, 1506−1519.
4. Storz, G., Altuvia, S., and Wassarman, K. M. (2005) An abundance of RNA regulators, *Annu. Rev. Biochem. 74*, 199−217.
5. Williamson, J. R. (2000) Induced fit in RNA-protein recognition, *Nat. Struct. Biol. 7*, 834−837.
6. Kim, H. D., Nienhaus, G. U., Ha, T., Orr, J. W., Williamson, J. R., and Chu, S. (2002) Mg2+-dependent conformational change of RNA studied by fluorescence correlation and FRET on immobilized single molecules, *Proc. Natl. Acad. Sci. U.S.A. 99*, 4284−4289.
7. Mu, Y., and Stock, G. (2006) Conformational dynamics of RNA-peptide binding: a molecular dynamics simulation study, *Biophys. J 90*, 391−399.
8. Zhang, Q., Sun, X., Watt, E. D., and Al-Hashimi, H. M. (2006) Resolving the motional modes that code for RNA adaptation, *Science 311*, 653−656.
9. Dayie, K. T., Brodsky, A. S., and Williamson, J. R. (2002) Base flexibility in HIV-2 TAR RNA mapped by solution (15)N, (13)C NMR relaxation, *J. Mol. Biol. 317*, 263−278.
10. Pitici, F., Beveridge, D. L., and Baranger, A. M. (2002) Molecular dynamics simulation studies of induced fit and conformational capture in U1A-RNA binding: do molecular substates code for specificity? *Biopolymers 65*, 424−435.
11. Noeske, J., Buck, J., Furtig, B., Nasiri, H. R., Schwalbe, H., and Wohnert, J. (2007) Interplay of 'induced fit' and preorganization in the ligand induced folding of the aptamer domain of the guanine binding riboswitch, *Nucleic Acids Res. 35*, 572−583.
12. Hermann, T., and Westhof, E. (1999) Simulations of the dynamics at an RNA-protein interface, *Nat. Struct. Biol. 6*, 540−544.
13. Muesing, M. A., Smith, D. H., and Capon, D. J. (1987) Regulation of mRNA accumilation by a human immunodeficiency virus trans-activator protein, *Cell 48*, 691−701.
14. Al-Hashimi, H. M., Gosser, Y., Gorin, A., Hu, W., Majumdar, A., and Patel, D. J. (2002) Concerted motions in HIV-1 TAR RNA may allow access to bound state conformations RNA dynamics from NMR residual dipolar couplings, *J. Mol. Biol. 315*, 95−102.
15. Weeks, K. M., Ampe, C., Schultz, S. C., Steitz, T. A., and Crothers, D. M. (1990) Fragments of the HIV-1 Tat protein specifically bind TAR RNA, *Science 249*, 1281−1285.
16. Bannwarth, S., and Gatignol, A. (2005) HIV-1 TAR RNA: the target of molecular interactions between the virus and its host, *Curr. HIV Res. 3*, 61−71.
17. Krebs, A., Ludwig, V., Boden, O., and Gobel, M. W. (2003) Targeting the HIV trans-activation responsive region−approaches towards RNA-binding drugs, *ChemBioChem 4*, 972−978.
18. Froeyen, M., and Herdewijn, P. (2002) RNA as a target for drug design, the example of Tat-TAR interaction, *Curr. Top. Med. Chem. 2*, 1123−1145.
19. Aboul-ela, F., Karn, J., and Varani, G. (1996) Structure of HIV-1 TAR RNA in the absence of ligands reveals a novel conformation of the trinucleotide bulge, *Nucleic Acids Res. 24*, 3974−3981.
20. Ippolito, J. A., and Steitz, T. A. (1998) A 1.3-angstrom resolution crystal structure of the HIV-1 trans- activation response region RNA stem reveals a metal ion-dependent bulge conformation, *Proc. Natl. Acad. Sci. U.S.A. 95*, 9819−9824.
21. Puglisi, J. D., Tan, R., Calnan, B. J., Frankel, A. D., and Williamson, J. R. (1992) Conformation of the TAR RNA-arginine complex by NMR spectroscopy, *Science 257*, 76−80.
22. Aboul-ela, F., Karn, J., and Varani, G. (1995) The structure of the human-immunodeficiency-virus type-1 Tar RNA reveals principles of RNA recognition by tat protein, *J. Mol. Biol. 253*, 313−332.
23. Faber, C., Sticht, H., Schweimer, K., and Rosch, P. (2000) Structural rearrangements of HIV-1 Tat-responsive RNA upon binding of neomycin B, *J. Biol. Chem. 275*, 20660−20666.
24. Du, Z., Lind, K. E., and James, T. L. (2002) Structure of TAR RNA complexed with a Tat-TAR interaction nanomolar inhibitor that was identified by computational screening, *Chem. Biol. 9*, 707−712.
25. Murchie, A. I., Davis, B., Isel, C., Afshar, M., Drysdale, M. J., Bower, J., Potter, A. J., Starkey, I. D., Swarbrick, T. M., Mirza, S., Prescott, C. D., Vaglio, P., Aboul-ela, F., and Karn, J. (2004) Structure-based drug design targeting an inactive RNA conforma-

tion: exploiting the flexibility of HIV-1 TAR RNA, *J. Mol. Biol. 336*, 625−638.
26. Davis, B., Afshar, M., Varani, G., Murchie, A. I., Karn, J., Lentzen, G., Drysdale, M., Bower, J., Potter, A. J., Starkey, I. D., Swarbrick, T., and Aboul-ela, F. (2004) Rational design of inhibitors of HIV-1 TAR RNA through the stabilisation of electrostatic "hot spots". *J. Mol. Biol. 336*, 343−356.
27. Chin, K., Sharp, K. A., Honig, B., and Pyle, A. M. (1999) Calculating the electrostatic properties of RNA provides new insights into molecular interactions and function, *Nat. Struct. Biol. 6*, 1055−1061.
28. Garcia-Garcia, C., and Draper, D. E. (2003) Electrostatic interactions in a peptide−RNA complex, *J. Mol. Biol. 331*, 75−88.
29. Woodson, S. A. (2005) Metal ions and RNA folding: a highly charged topic with a dynamic future, *Curr. Opin. Chem. Biol. 9*, 104−109.
30. Draper, D. E., Grilley, D., and Soto, A. M. (2005) Ions and RNA folding, *Annu. Rev. Biophys. Biomol. Struct. 34*, 221−243.
31. Draper, D. E. (2004) A guide to ions and RNA structure, *RNA 10*, 335−343.
32. Law, M. J., Linde, M. E., Chambers, E. J., Oubridge, C., Katsamba, P. S., Nilsson, L., Haworth, I. S., and Laird-Offringa, I. A. (2006) The role of positively charged amino acids and electrostatic interactions in the complex of U1A protein and U1 hairpin II RNA, *Nucleic Acids Res. 34*, 275−285.
33. Tao, J., and Frankel, A. D. (1993) Electrostatic interactions modulate the RNA-binding and transactivation specificities of the human immunodeficiency virus and simian immunodeficiency virus Tat proteins, *Proc. Natl. Acad. Sci. U.S.A. 90*, 1571−1575.
34. Blount, K. F., and Tor, Y. (2003) Using pyrene-labeled HIV-1 TAR to measure RNA-small molecule binding, *Nucleic Acids Res. 31*, 5490−5500.
35. Pitt, S. W., Zhang, Q., Patel, D. J., and Al-Hashimi, H. M. (2005) Evidence that electrostatic interactions dictate the ligand-induced arrest of RNA global flexibility, *Angew. Chem., Int. Ed. 44*, 3412−3415.
36. Olejniczak, M., Gdaniec, Z., Fischer, A., Grabarkiewicz, T., Bielecki, L., and Adamiak, R. W. (2002) The bulge region of HIV-1 TAR RNA binds metal ions in solution, *Nucleic Acids Res. 30*, 4241−4249.
37. Edwards, T. E., and Sigurdsson, S. T. (2003) EPR spectroscopic analysis of TAR RNA-metal ion interactions, *Biochem. Biophys. Res. Commun. 303*, 721−725.
38. Edwards, T. E., Okonogi, T. M., and Sigurdsson, S. T. (2002) Investigation of RNA-protein and RNA-metal ion interactions by electron paramagnetic resonance spectroscopy. The HIV TAR-Tat motif, *Chem. Biol. 9*, 699−706.
39. Zacharias, M., and Hagerman, P. J. (1995) The bend in RNA created by the transactivation response element bulge of human-immunodeficiency-virus is straightened by arginine and by Tat-derived peptide, *Proc. Natl. Acad. Sci. U.S.A. 92*, 6052−6056.
40. Al-Hashimi, H. M., Pitt, S. W., Majumdar, A., Xu, W., and Patel, D. J. (2003) Mg2+-induced variations in the conformation and dynamics of HIV-1 TAR RNA probed using NMR residual dipolar couplings, *J. Mol. Biol. 329*, 867−873.
41. Zacharias, M., and Hagerman, P. J. (1995) Bulge-induced bends in RNA: quantification by transient electric birefringence, *J. Mol. Biol. 247*, 486−500.
42. Bokinsky, G., and Zhuang, X. (2005) Single-molecule RNA folding, *Acc. Chem. Res. 38*, 566−573.
43. Brenowitz, M., Chance, M. R., Dhavan, G., and Takamoto, K. (2002) Probing the structural dynamics of nucleic acids by quantitative time-resolved and equilibrium hydroxyl radical "footprinting", *Curr. Opin. Struct. Biol. 12*, 648−653.
44. Takamoto, K., He, Q., Morris, S., Chance, M. R., and Brenowitz, M. (2002) Monovalent cations mediate formation of native tertiary structure of the *Tetrahymena thermophila* ribozyme, *Nat. Struct. Biol. 9*, 928−933.
45. Caliskan, G., Hyeon, C., Perez-Salas, U., Briber, R. M., Woodson, S. A., and Thirumalai, D. (2005) Persistence length changes dramatically as RNA folds, *Phys. Rev. Lett. 95*, 268303−1−26830.3−4.
46. Perez-Salas, U. A., Rangan, P., Krueger, S., Briber, R. M., Thirumalai, D., and Woodson, S. A. (2004) Compaction of a bacterial group I ribozyme coincides with the assembly of core helices, *Biochemistry 43*, 1746−1753.
47. Mollova, E. T., and Pardi, A. (2000) NMR solution structure determination of RNAs, *Curr. Opin. Struct. Biol. 10*, 298−302.
48. Al-Hashimi, H. M., Gorin, A., Majumdar, A., Gosser, Y., and Patel, D. J. (2002) Towards structural genomics of RNA: rapid NMR resonance assignment and simultaneous RNA tertiary structure determination using residual dipolar couplings, *J. Mol. Biol. 318*, 637−649.
49. Al-Hashimi, H. M., and Patel, D. J. (2002) Residual dipolar couplings: synergy between NMR and structural genomics, *J. Biomol. NMR 22*, 1−8.
50. Tolman, J. R., Flanagan, J. M., Kennedy, M. A., and Prestegard, J. H. (1995) Nuclear magnetic dipole interactions in field-oriented proteins: information for structure determination in solution, *Proc. Natl. Acad. Sci. U.S.A. 92*, 9279−9283.
51. Tjandra, N., and Bax, A. (1997) Direct measurement of distances and angles in biomolecules by NMR in a dilute liquid crystalline medium, *Science 278*, 1111−1114.
52. Prestegard, J. H., Al-Hashimi, H. M., and Tolman, J. R. (2000) NMR structures of biomolecules using field oriented media and residual dipolar couplings, *Q. Rev. Biophys. 33*, 371−424.
53. Bax, A., and Grishaev, A. (2005) Weak alignment NMR: a hawk-eyed view of biomolecular structure, *Curr. Opin. Struct. Biol. 15*, 563−570.
54. Mollova, E. T., Hansen, M. R., and Pardi, A. (2000) Global structure of RNA determined with residual dipolar couplings, *J. Am. Chem. Soc. 122*, 11561−11562.
55. Musselman, C., Pitt, S. W., Gulati, K., Foster, L. L., Andricioaei, I., and Al-Hashimi, H. M. (2006) Impact of static and dynamic A-form heterogeneity on the determination of RNA global structural dynamics using NMR residual dipolar couplings, *J. Biomol. NMR 36*, 235−249.
56. Hansen, M. R., Hanson, P., and Pardi, A. (2000) Filamentous bacteriophage for aligning RNA, DNA, and proteins for measurement of nuclear magnetic resonance dipolar coupling interactions, *Methods Enzymol. 317*, 220−240.
57. Clore, G. M., Starich, M. R., and Gronenborn, A. M. (1998) Measurement of residual dipolar couplings of macromolecules aligned in the nematic phase of a colloidal suspension of rod-shaped viruses, *J. Am. Chem. Soc. 120*, 10571−10572.
58. Delaglio, F., Grzesiek, S., Vuister, G. W., Zhu, G., Pfeifer, J., and Bax, A. (1995) Nmrpipe - a multidimensional spectral processing system based on unix pipes, *J. Biomol. NMR 6*, 277−293.
59. Goddard, T. D., and Kneller, D. G. *SPARKY 3*, University of California, San Franscisco, CA, 2004.
60. Meissner, A., and Sorensen, O. W. (1999) The role of coherence transfer efficiency in design of TROSY- type multidimensional NMR experiments, *J. Magn. Reson. 139*, 439−442.
61. Neidle, S. (1999) *Oxford Handbook of Nucleic Acid Structure*, Oxford University Press, New York.
62. Losonczi, J. A., Andrec, M., Fischer, M. W. F., and Prestegard, J. H. (1999) Order matrix analysis of residual dipolar couplings using singular value decomposition, *J. Magn. Reson. 138*, 334−342.
63. Hansen, A. L., and Al-Hashimi, H. M. (2006) Insight into the CSA tensors of nucleobase carbons in RNA polynucleotides from solution measurements of residual CSA: towards new long-range orientational constraints, *J. Magn. Reson. 179*, 299−307.
64. Al-Hashimi, H. M., Valafar, H., Terrell, M., Zartler, E. R., Eidsness, M. K., and Prestegard, J. H. (2000) Variation of molecular alignment as a means of resolving orientational ambiguities in protein structures from dipolar couplings, *J. Magn. Reson. 143*, 402−406.
65. Gonzalez, R. L., Jr., and Tinoco, I., Jr. (1999) Solution structure and thermodynamics of a divalent metal ion binding site in an RNA pseudoknot, *J. Mol. Biol. 289*, 1267−1282.
66. Nicholls, A., Sharp, K., and Honig, B. (1991) Protein folding and association:insights from the interfacial and thermodynamic properties of hydrocarbons, *Proteins 11*, 281−296.
67. Cornell, W. D., Cieplak, P., Bayly, C. I., Gould, I. R., Merz, K. M., Ferguson, D. M., Spellmeyer, D. C., Fox, T., Caldwell, J. W., and Kollman, P. A. (1995) A 2nd generation force-field for the simulation of proteins, nucleic-acids, and organic-molecules, *J. Am. Chem. Soc. 117*, 5179−5197.
68. Saupe, A. (1968) Recent results in the field of liquid crystals, *Angew. Chem., Int. Ed. Engl. 7*, 97−112.
69. Tolman, J. R., Al-Hashimi, H. M., Kay, L. E., and Prestegard, J. H. (2001) Structural and dynamic analysis of residual dipolar coupling data for proteins, *J. Am. Chem. Soc. 123*, 1416−1424.
70. Zhang, Q., Throolin, R., Pitt, S. W., Serganov, A., and Al-Hashimi, H. M. (2003) Probing motions between equivalent RNA domains

using magnetic field induced residual dipolar couplings: accounting for correlations between motions and alignment, *J. Am. Chem. Soc. 125*, 10530−10531.
71. Bolon, P. J., Al-Hashimi, H. M., and Prestegard, J. H. (1999) Residual dipolar coupling derived orientational constraints on ligand geometry in a 53 kDa protein-ligand complex, *J. Mol. Biol. 293*, 107−115.
72. Pitt, S. W., Majumdar, A., Serganov, A., Patel, D. J., and Al-Hashimi, H. M. (2004) Argininamide binding arrests global motions in HIV-1 TAR RNA: comparison with Mg2+-induced conformational stabilization, *J. Mol. Biol. 338*, 7−16.

BI700335N